ACCEPTED VERSION

Stephan Kruse, Paul Medwell, Marco Davidovic, Zhiwei Sun, Jingjing Ye, Heinz Pitsch, Bassam Dally
The effect of fuel composition and Reynolds number on soot formation processes in turbulent non-premixed toluene jet flames

Final publication at: http://dx.doi.org/10.1016/j.proci.2020.06.140

PERMISSIONS

https://www.elsevier.com/about/policies/sharing

Accepted Manuscript

Authors can share their accepted manuscript:

24 Month Embargo

After the embargo period

- via non-commercial hosting platforms such as their institutional repository
- via commercial sites with which Elsevier has an agreement

In all cases accepted manuscripts should:

- link to the formal publication via its DOI
- bear a CC-BY-NC-ND license – this is easy to do
- if aggregated with other manuscripts, for example in a repository or other site, be shared in alignment with our hosting policy
- not be added to or enhanced in any way to appear more like, or to substitute for, the published journal article

12 April 2023

---

http://hdl.handle.net/2440/128967

The effect of fuel composition and Reynolds number on soot formation processes in turbulent non-premixed toluene jet flames

Stephan Kruse[a,*], Paul Medwell[b], Marco Davidovic[a], Zhiwei Sun[b], Jingjing Ye[b], Heinz Pitsch[a], Bassam Dally[b]

[a]*Institute for Combustion Technology - RWTH Aachen University, Templergraben 64, Aachen 52062, Germany*
[b]*School of Mechanical Engineering - The University of Adelaide, S.A. 5005, Australia*

Abstract

The soot formation processes in three different turbulent prevaporized non-premixed toluene jet flames stabilized on a jet-in-hot-coflow (JHC) burner were investigated in this study. The jet Reynolds number and the stoichiometric mixture fraction were varied in order to manipulate the flow time scales and the chemistry, respectively. Time-resolved laser-induced incandescence (TiRe-LII), non-linear two-line atomic fluorescence of indium (nT-LAF), and OH planar laser induced fluorescence (PLIF) were simultaneously applied to yield spatially resolved and instantaneous fields of soot volume fraction, primary particle size, temperature, and OH. The mean distributions of the detected quantities are used to identify major differences among the flames. The highest soot loading is observed for the low Reynolds number and low stoichiometric mixture fraction flame. However, this flame features also the lowest temperature and primary particle size. Based on these ob-

*Corresponding author: s.kruse@itv.rwth-aachen.de

servations, the simultaneously detected data sets and flamelet computations are employed to elucidate differences in the soot formation pathways in the flames. The analyses reveal that the high soot loading causes greater heat losses in the low Reynolds number and low stoichiometric mixture fraction flame. This has a significant impact on the soot formation pathways and causes a reduction in the particle size.

1. Introduction

Soot formation is a highly complex multi-phase and multi-scale process and is one of the least understood processes in combustion research [1]. In most practical combustion systems, soot is an undesired combustion product that causes adverse effects on global climate and human health [2]. Nonetheless, in few others soot is highly desirable as it enhances thermal radiation like in boilers and furnaces.

Fundamental knowledge of the soot formation processes has mostly been gained from detailed experimental and numerical studies in laminar flames [3]. However, in light of the complex and non-linear correlation of turbulence, chemical kinetics, and soot formation processes, detailed simulations [4, 5] and advanced experimental studies [6, 7] of turbulent sooting flames have also been performed.

Several experimental studies on turbulent flames examined the impact of large-scale parameters on soot formation. Lee et al. [8] investigated the

effect of the fuel jet Reynolds number on the formation of soot in a turbulent ethylene/air diffusion flame. With increasing turbulence level, a reduction in the overall soot production and a broader radial soot distribution was observed. A study by Mahmoud et al. [9] on soot formation in a turbulent ethylene flame with varying Reynolds numbers and constant strain rate revealed a strong increase of the integrated soot volume fraction (f_v) with larger Reynolds numbers. The significant increase of the integrated f_v was attributed to the increase of the flame volume with the Reynolds number. The increase of the jet strain rate for constant Reynolds numbers was found to decrease f_v locally and globally in the flame [10]. Recently, the impact of the air flow rate on soot formation in a swirl-stabilized methane flame was investigated by Wang et al. [11]. While the time-averaged f_v decreases and the soot intermittency increases by the increase of the air flow rate, the primary soot particle size (d_p) remains unaffected by the air flow rate.

Detailed analysis on correlations of local soot quantities and local flame properties have been mostly deduced from direct numerical simulations (DNS) of ethylene [4] and n-heptane [5, 12] jet flames. Lignell et al. [4] reported a strong correlation of the local flame curvature on the soot transport relative to the flame surface. From DNS data of a turbulent n-heptane jet, differential diffusion between soot and gas-phase species was identified to have a significant impact on the soot distribution in mixture fraction space and on its formation mechanisms [13]. This observation was confirmed by an experimental investigation of the soot inception region of a turbulent ethylene flame performed by Park et al. [14]. These observations reinforce the need for detection of key scalars in the flame, simultaneously with soot quantities,

to elucidate the soot formation processes in turbulent flames.

Toluene is a typical component in gasoline and Diesel surrogates to mimic the aromatic content and ignition behavior of conventional fuels [15]. As its molecular structure consists of an aromatic six-carbon ring with an additional methyl group, toluene favors soot formation [16]. Preliminary studies on turbulent toluene and turbulent n-heptane/toluene jet flames with focus on the soot formation and oxidation process, and the soot evolution in a hot vitiated coflow were reported recently [17, 18].

The paper targets the urgent demand of flame and soot quantities from practical fuel component in a turbulent environment. Multiple simultaneously employed laser diagnostics are used to reveal novel insights into the complex correlation of temperature and soot quantities in turbulent toluene flames. Moreover, the joint statistics of temperature and soot data accompanied by flamelet computations provide novel insights into the effect of soot radiation on the soot formation pathways.

2. Experimental and numerical methods

The well-established Jet-in-Hot-Coflow (JHC) burner, that has been widely used in studies of Moderate or Intense Low oxygen Dilution (MILD) and on soot formation, was employed in the current work [18]. In the JHC burner, the turbulent fuel jet is injected from a nozzle with a diameter of 4.6 mm into a hot and vitiated coflow. The hot coflow emerges from a lean premixed natural gas flame that is stabilized on a porous burner approximately 25 mm upstream of the jet exit. The coflow flame has a diameter of 110 mm and is surrounded by a 22 mm wide annular channel for the air shielding flow. A

4

detailed description of the JHC configuration is provided in Ref. [18]. The burner was mounted on a translation stage that enabled measurements at locations of up to 345 mm above the jet exit plane. The fuel was controlled by a Coriolis mass flow controller (mini Cori-Flow, Bronkhorst), mixed with N_2 and evaporated in an evaporation unit (CEM, Bronkhorst). The lines between evaporation unit and burner inlet were heated to achieve a temperature of 453 K at the jet exit plane. The natural gas, air, and N_2 flow of the coflow were adjusted by mass flow controllers to maintain a temperature of 1544 K and an oxygen mass fraction of 8.33 % in the product stream. The shielding flow exit velocity was set to 0.8 m/s.

The current optical setup has been frequently used for simultaneous measurements of soot and T distribution [7, 16]. Therefore, only a brief description of the optical setup is given herein. The arrangement of the optical components is schematically shown in Fig. 1. The local temperature was determined from the atomic fluorescence signal of indium. Indium nanoparticles from a rod ablation technique were seeded to the fuel upstream of the burner inlet. Indium is excited by two laser beams with wavelengths of 450 nm and 410 nm. The two beams were combined and formed to a light sheet. Two intensified CCD cameras (PI-Max4, Princeton Instruments) equipped with bandpass filters of 451.4 nm (FWHM = 1.32 nm) and 410.4 nm (FWHM = 1.08 nm) were employed to detect the Stokes and Anti-Stokes signal, respectively. The exposure times were 30 ns. The images were corrected for spatial and temporal fluence fluctuations in the light sheet on a shot-to-shot basis. For signal calibration, nTLAF and thermocouple measurements were performed daily in a well-characterized flat flame Hencken-type burner. The

uncertainties in T have been previously reported to $\pm 120\,\mathrm{K}$ [19].

The local d_p and f_v were determined from TiRe-LII measurements. The fundamental ($1064\,\mathrm{nm}$) of a Nd:YAG-laser (Brilliant B, Quantel) was formed to a light sheet and combined with the nTLAF sheet. The laser energy output was set to achieve an averaged sheet fluence of $0.3\,\mathrm{J/cm^2}$. The LII signal was recorded by a camera system (HSFC Pro, pco) equipped with a Nikon f/1.4 camera and a bandpass filter ($435\,\mathrm{nm}$, FWHM = $48.8\,\mathrm{nm}$). The gating time for each camera was set to $40\,\mathrm{ns}$. Then, the LII signal decay was recorded by a sequence of four images, where the first image was recorded prompt with the LII beam and the subsequent ones $80\,\mathrm{ns}$, $160\,\mathrm{ns}$, and $240\,\mathrm{ns}$ after the laser beam. The first image yields the local f_v, whereas
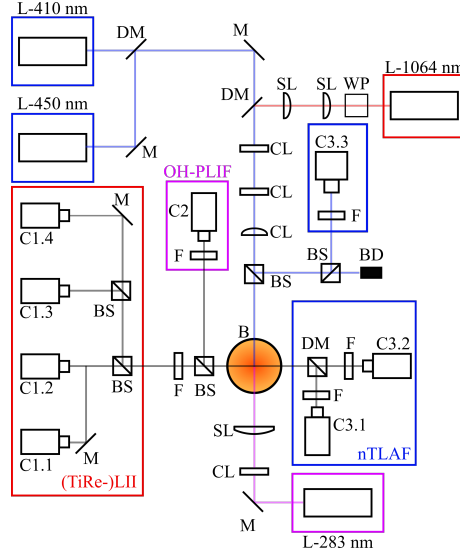

Figure 1: Optical arrangement at the University of Adelaide which includes: (TiRe-) LII, OH-PLIF, and nTLAF for time-resolved simultaneous detection of f_v, d_p, T, and OH. BD, beam dump; BS, beam splitter; C, camera; CL, cylindrical lens; DM, dichroic mirror; F, filter; L, laser; M, mirror; SL, spherical lens; WP, wave plate and polarization filter.

the ratios of the sequential images were used to derive d_p. The LII signals were calibrated against extinction measurements in a Santoro flame. The uncertainty of f_v was determined to be $\pm 10\%$. Details on the modeling of the decay curve and the TiRe-LII data quantification are provided in Ref. [20]. The assumptions of non-aggregated, mono-disperse soot particles in the signal decay model induces an overestimation of the particle size by a factor of two. From measurements in McKenna type flames [20], the detection limit of the current TiRe-LII setup was determined to be approximately d_p = 5 nm. Measurements in a Santoro flame revealed an uncertainty in d_p measurements of $\pm 20\%$.

For visualization of the reaction zone, OH-PLIF is used. To avoid signal interference between the different laser-based techniques, the detection sequence was nTLAF, OH-PLIF, and TiRe-LII with delays of $1\,\mu$s and $2\,\mu$s, respectively. All images were spatially matched by a target image and corrected for background signal, chip inhomogeneities, and vignetting. The in-plane resolution was 0.0887 mm/Pixel and the field of view was 14 mm high.

The experiments are accompanied by unsteady flamelet computations. An in-house chemistry solver is used to solve the unsteady non-premixed flamelet equations for unity Lewis number. An error function profile is imposed as functional form of the scalar dissipation rate. Soot evolution is calculated using the Hybrid Method of Moments (HMOM) model [21], while the soot moment equations are solved in mixture fraction space [22]. The soot model accounts for nucleation, condensation, coagulation, surface growth, oxidation, and thermophoretic transport, while soot particle diffusion has been

neglected. Furthermore, soot [23] and gas phase radiation is considered. The simulations are initialized by adiabatic mixing of fuel and oxidizer. The mixture is ignited by assuming complete conversion of fuel to water and carbon dioxide. The initial temperature is calculated from enthalpy given the species composition.

3. Results and Discussion

Three different turbulent toluene flames with varying Z_{st} and fuel-jet Reynolds number (Re_F) were investigated. In the absence of detailed flow field measurements, the Reynolds number is utilized as a characteristic non-dimensional parameter of the flow field to distinguish the three different flames. Z_{st} is varied by changing the fuel mass fraction in the fuel/N_2-jet and Re_F is adjusted by modification of the fuel jet exit velocity. The experimental boundary conditions of the flames are summarized in Table 1 and photographs of each flame are shown in Fig. 2. The flame length (L_F) was determined from flame videos. An analytic correlation by Hawthorne et al. [24] suggests that the flame length L_F is proportional to the nozzle diameter and also scales inversely with Z_{st}. In order to consider the change in Z_{st}, the axial distance is normalized by L_F to consider variations in the flame length introduced by variation of Z_{st}.

The photographs highlight the independence of the flame length from the fuel jet Reynolds number (Fig 2b & Fig. 2c), whereas a significant increase of the flame length with a reduction of Z_{st} is evident from Fig. 2a & Fig. 2b.

8

Table 1: Summary of the experimental conditions and flame' length (L_F). Flame Y25-R10 has also been subject in a study of soot oxidation [17].

Case label	Re_F	Y_F	Z_{st}	L_F [mm]
Y25-R10	10.000	0.25	0.230	400
Y35-R10	10.000	0.35	0.175	490
Y35-R15	15.000	0.35	0.175	490

3.1. Ensemble-averaged data analysis

The mean distributions of the simultaneously recorded temperature, OH, f_v, and d_p fields were determined from 499 individual images of each quantity. The mean $\langle f_v \rangle$ at each measurement location is presented in Fig. 3. Soot is initially detected in flame Y35-R10 at around 50 mm above the jet exit,
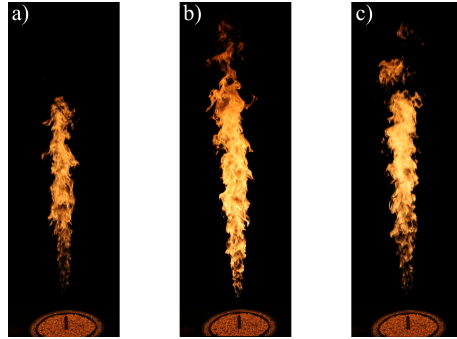

Figure 2: Photographs of the three investigated flames a) Y25-R10, b) Y35-R10, and c) Y35-R15. The photographs were recorded with a digital reflex camera (Canon EOS 700). The setting remained constant for each photograph, f/4 and exposure time 1/4000 s.
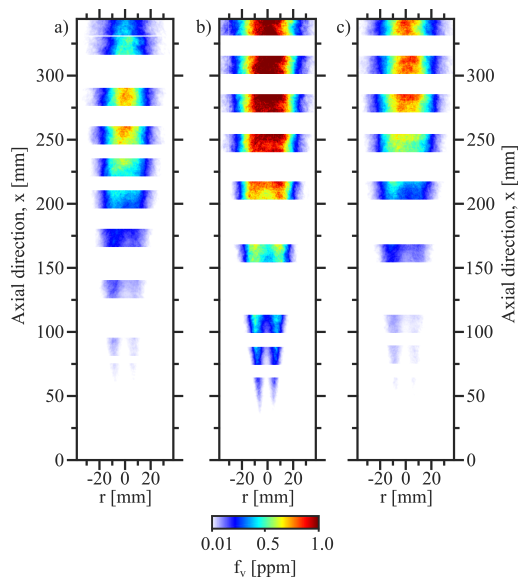
Figure 3: $\langle f_v \rangle$ from LII measurements at several heights above the jet exit plane for the three investigated flames: a) Y25-R10, b) Y35-R10, c) Y35-R15.

whereas an increase in Z_{st} (Y25-R10) and an increase in the jet Reynolds number (Y35-R10) delays soot inception. Soot inception occurs in confined regions away from the centerline and spreads towards the centerline with increasing axial distance. Over the entire flame length, the maximum $\langle f_v \rangle$ is found for flame Y35-R10. Further downstream, soot is transported by the turbulent flow field [25] resulting in a wide radial distribution of soot and a peak of $\langle f_v \rangle$ at the centerline. For flame Y25-R10, this characteristic soot distribution is observed at $x = 250$ mm. A reduction of Z_{st} results in a shift of this flame region further downstream ($x = 300$ mm). For flame Y25-R10, soot oxidation reduces $\langle f_v \rangle$ for $x \geq 250$ mm [17].

Figure 4 presents the soot intermittency at the centerline along the flame axis. The intermittency factor is defined as the probability of soot to not
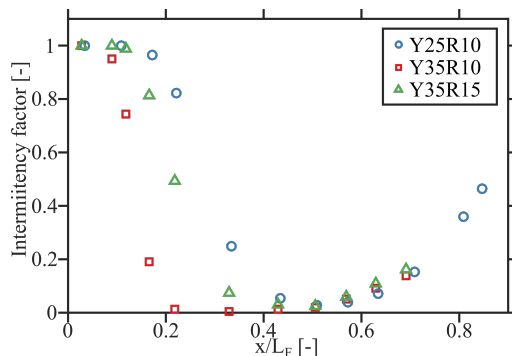
10

Figure 4: Axial profile of intermittency factor determined at centerline along burner axis.

be detected at a certain location [26]. Hence, an intermittency factor of one implies the permanent presence of soot. The intermittency curves in Fig. 4 exhibit a similar characteristic for all flames. After inception, the soot presence on the centerline increases and soot is permanently present in the range of $x/L_F = 0.4$-0.5. Thereafter, the intermittency on the centerline increases with downstream direction. Generally, the trend is consistent with the overall soot loading in the flame. The lowest intermittency is found for flame Y35-R10, whereas an elevated turbulence (Y35-R15) level and increased Z_{st} increase the intermittency in the soot inception region. Figure 5 presents the radial mean profiles of the ensemble-averaged soot quantities, temperature, and normalized OH signal at $x/L_F = 0.32$ and $x/L_F = 0.62$. The first position is close to the soot inception region and ensures sufficiently large simultaneous data sets of all quantities for the later statistical analysis. At $x/L_F = 0.62$, the flame and soot formation are fully developed, but soot oxidation is still absent. The OH signal has not been corrected for local quenching and fluctuations of the excitation beam energy. Therefore, the mean OH profiles in Fig. 5 are normalized to their corresponding maximum
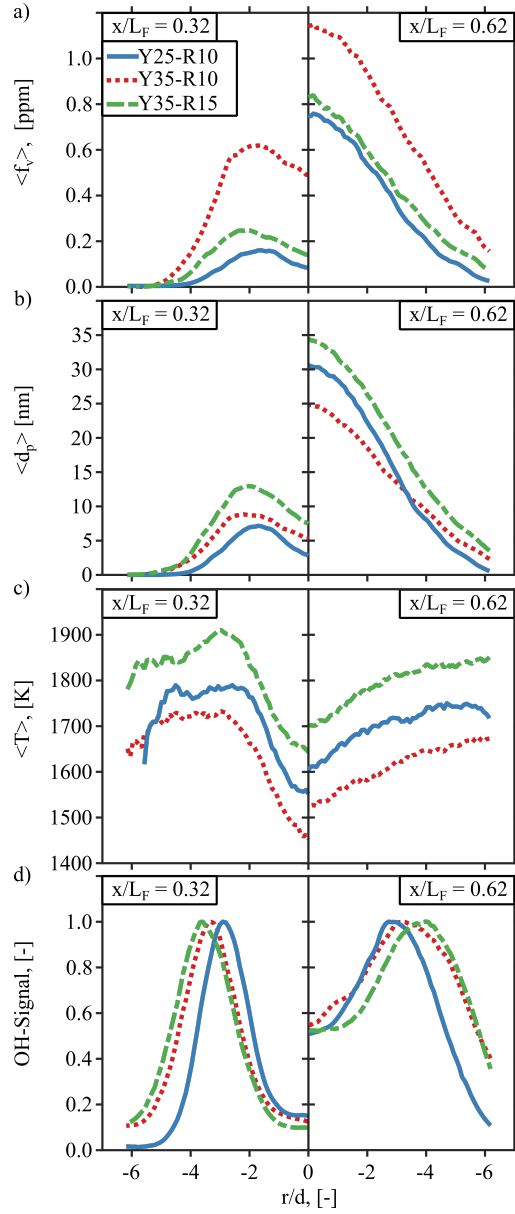
11

Figure 5: Radial profiles of ensemble-averaged a) $\langle f_v \rangle$, b) $\langle d_p \rangle$, c) $\langle T \rangle$, and d) normalized OH-signal at $x/L_F = 0.32$ and $x/L_F = 0.62$ for the three investigated flames.

signal and indicate a shift of the OH peak in radial direction with decreasing Z_{st} at x/L_F=0.32. The increase of the flame Reynolds number moves the flame position further outwards. The lowest temperature is observed for flame Y35-R10, while the high Reynolds number jet flame yields the highest temperature. The nTLAF technique is limited to temperatures above $800\,\mathrm{K}$, $\langle T \rangle$ is inherently conditioned to data above $800\,\mathrm{K}$. This might also explain the elevated $\langle T \rangle$ at the jet centerline at $x/L_F = 0.32$. In addition, as indium is rapidly oxidized in the presence of oxygen, profiles of $\langle T \rangle$ beyond the OH peak might be attributed to a few instantaneous events where the OH layer is shifted outwards. At $x/L_F = 0.32$, the profiles of $\langle f_v \rangle$ and $\langle d_p \rangle$ reveal that soot is limited to the region between centerline and OH layer. Note that values of d_p below the detection limit of $5\,\mathrm{nm}$ were considered as zero in the determination of the mean value. Hence, mean values of d_p below the detection limit of $5\,\mathrm{nm}$ are a result of the unconditioned ensemble-averaging. The maximum $\langle f_v \rangle$ is found in flame Y35-R10, where the larger time scales and the reduced mixing with oxygen benefit the soot formation. The peaks of $\langle f_v \rangle$ and $\langle d_p \rangle$ follow the trend of the OH peaks. For flame Y25-R10, the peak is located closest to the centerline, hence close to the turbulent core of the fuel jet. Here, the small flow time scales reduce soot formation further and contribute to the elevated intermittency. It is remarkable that flame Y35-R10 yields the highest $\langle f_v \rangle$, but $\langle d_p \rangle$ is less than that of flame Y35-R15. With increasing axial distance, the radial profiles exhibit a broader distribution of all measured quantities. The OH peak is transferred to outer radial locations with OH also present on the centerline. While the mean profiles of $\langle T \rangle$ are flatter as compared to those obtained at $x/L_F = 0.32$. Even lower

13

temperatures are observed for flame Y35-R10. The peaks of $\langle f_v \rangle$ and $\langle d_p \rangle$ are located at the centerline. In radial direction, $\langle f_v \rangle$ and $\langle d_p \rangle$ gradually decrease, whereas flame Y35-R10 yields the maximum $\langle f_v \rangle$. Consistent with the observations at $x/L = 0.32$, the minimum $\langle d_p \rangle$ is observed for flame Y35-R10 at the jet centerline. This characteristic will be further analyzed in the subsequent section.

3.2. Soot and temperature statistics

As beam steering is well-known to induce significant errors on the LII measurements in turbulent flames [20], the discussion in this section is based on data that are obtained from the half of the image on the beam entrance side. Heat loss via radiation is suspected as the major source for the reduced T in flame Y35-R10. Therefore, the heat loss from soot radiation is computed from simultaneously detected T and f_v data. Based on the work by Liu et al. [27], the heat loss via soot radiation is calculated by

$$q_{rad,soot} = 3.337 \times 10^{-4} f_v T^5, \tag{1}$$

where $q_{rad,soot}$ represents the heat loss in W/m^3. As the heat loss in turbulent toluene/n-heptane flames from gas radiation was found to be substantially lower compared with soot radiation [18], gas radiation is not considered here. Figure 6 shows the heat loss along the jet axis. Within the soot inception region, a higher heat loss is observed for flame Y35-R10 as compared to the other flames which in consequence has a profound impact on the flame temperature.

In order to qualitatively demonstrate the impact of radiation on soot formation, unsteady flamelet computations were performed with and without
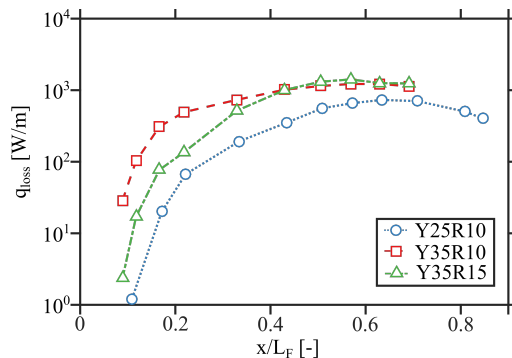
Figure 6: Radiative heat loss from soot along the burner axis for the three investigated flames.

soot radiation. In order to mimic the Reynolds number and Z_{st} variations, the flamelets were computed for different dissipation rates and fuel compositions. The temporal evolution of the peak f_v is shown in Fig. 7a. Note that the time axis can be interpreted as soot evolution along the flame axis. The soot formation is lowered by radiative heat loss for all flames (Fig. 7a). However, the reduction correlates with the soot loading and is highest for the flame with low dissipation rate and elevated fuel mass fraction. Moreover, the source terms for nucleation and condensation are also affected by soot radiation (Fig. 7b). Generally, soot originates in the high temperature region where the source term for nucleation is large. The dominant pathway for soot growth is condensation, which occurs over the entire range of T. Figure 7 demonstrates that the source term for nucleation is only slightly affected by radiation, whereas condensation is significantly reduced. This might particularly affect soot formation in flame Y35-R10, where radiation is substantial. Therefore, Fig. 8 presents probability density functions (pdf) of d_p and f_v conditioned to different ranges of T at $x/L_F = 0.32$. It is evident
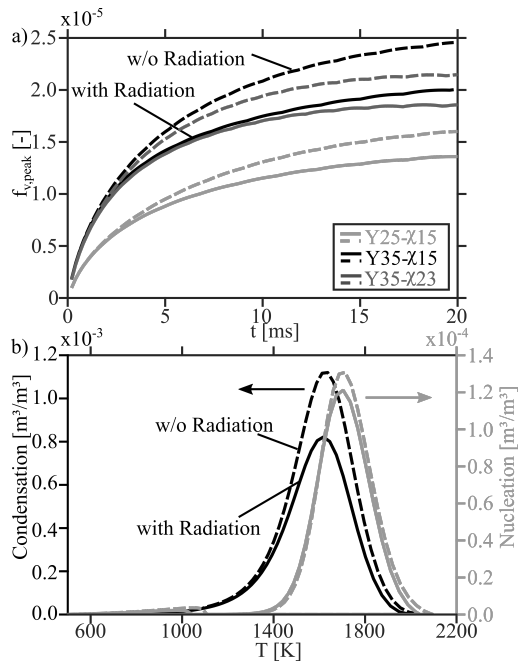
15

Figure 7: Temporal evolution of peak f_v for different fuel mass fractions and dissipation rates (χ) (a). Temperature dependence of source terms for condensation and nucleation with and without (w/o) radiation from flame $Y_F = 0.35$ and $\chi = 15\,\mathrm{s}^{-1}$.
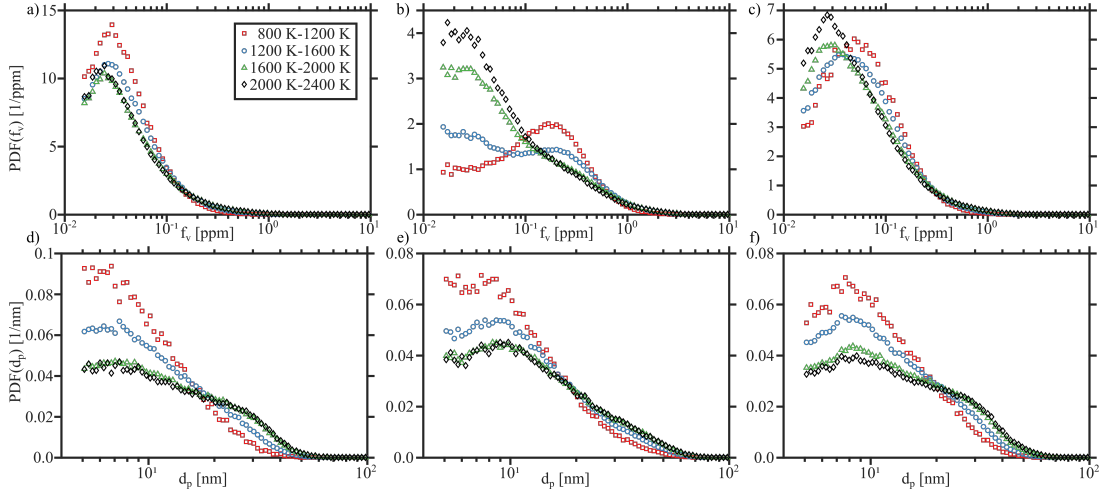
Figure 8: Pdfs of f_v and d_p conditioned to T for the investigated flames Y25-R10 (a & d), Y35-R10 (b & e), and Y35-R15 (c & f). Pdfs are determined at $x/L_F = 0.32$.

that soot is present in the entire temperature range. Consistent with the overall soot loading of the different flames, the range of the f_v pdfs increases from flame Y25-R10 towards Y35-R10. However, the temperature shift of the pdfs for the different flames is remarkable. While the f_v pdfs of flame Y25-R10 are nearly insensitive to T, a shift towards high f_v for decreasing T is observed for the pdfs of the two other flames. The effect is particularly pronounced for flame Y35-R10, where the probability of large f_v is increased for the low T-range. This characteristic is attributed to elevated soot formation in the flames with low Z_{st} where part of the soot, instead of being oxidized, is transported towards the fuel side and thus low T. In light of the lower d_p of flame Y35-R10 (Fig. 5), the distribution of d_p with respect to T is shown Figs. 8d-f. The maximum d_p is lowest for flame Y25-R10. For the two flames with low Z_{st}, d_p covers a similar range. However, differences are observed in the shape of the pdfs at elevated T. In the high temperature bands in flames

17

Y25-R10 and Y35-R15, the probability of small d_p is highest. Nonetheless, the probability for particles with d_p up to $\approx 30\,\text{nm}$ remains large. In contrast, the d_p pdf in flame Y35R10 gradually decreases for particles larger than $10\,\text{nm}$. The elevated probability of small particles in combination with the lower probability of large particles in flame Y35-R10 suggests that soot is formed by nucleation but particle growth via condensation is abated. This is consistent with reduced condensation rates at high T due to soot radiation (Fig. 7b).

4. Conclusion

Following the urgent demand of soot and flame quantities from practical fuel components, this study elaborates the soot formation of three turbulent toluene jet flames with different Reynolds numbers and Z_{st}. Four different laser-based diagnostics were simultaneously employed to extract instantaneous and spatially resolved information on T, f_v, d_p, and reaction layer from the turbulent flames. This complex data set provides profound knowledge on the relationship of temperature and soot quantities. Ensemble-averaged data revealed a lower soot loading with reduced flow times scales and larger Z_{st}. For constant Z_{st}, a decrease of the jet Reynolds number increases the mean f_v, whereas d_p and T are reduced. The reduced T is ascribed to significantly higher heat losses via radiation. As soot loading is significantly higher in the low Reynolds number jet, pdfs of f_v and d_p conditioned to T indicate the transport of soot towards lower T for the reduced Z_{st}. The pdf of d_p at high T for the most sooting flame indicates a significantly higher probability of small particles in comparison to larger particles. This characteristic is con-

18

sistent with the flamelet computations that suggest a reduced soot growth via condensation with elevated soot radiation.

Acknowledgments

References

[1] H. Michelsen, Probing soot formation, chemical and physical evolution, and oxidation: A review of in situ diagnostic techniques and needs, Proc. Combust. Inst. 36 (1) (2017) 717 – 735.

[2] M. Heal, P. Kumar, R. Harrison, Particles, air quality, policy and health, Chem. Soc. Rev. 41 (19) (2012) 6606–6630.

[3] H. Wang, Formation of nascent soot and other condensed-phase materials in flames, Proc. Combust. Inst. 33 (1) (2011) 41 – 67.

[4] D. O. Lignell, J. H. Chen, P. J. Smith, Three-dimensional direct numerical simulation of soot formation and transport in a temporally evolving

nonpremixed ethylene jet flame, Combust. Flame 155 (1) (2008) 316 – 333.

[5] A. Attili, F. Bisetti, M. E. Mueller, H. Pitsch, Formation, growth, and transport of soot in a three-dimensional turbulent non-premixed jet flame, Combust. Flame 161 (7) (2014) 1849 – 1865.

[6] M. Köhler, K.-P. Geigle, T. Blacha, P. Gerlinger, W. Meier, Experimental characterization and numerical simulation of a sooting lifted turbulent jet diffusion flame, Combust. Flame 159 (8) (2012) 2620 – 2635.

[7] D. Gu, Z. Sun, B. B. Dally, P. R. Medwell, Z. T. Alwahabi, G. J. Nathan, Simultaneous measurements of gas temperature, soot volume fraction and primary particle diameter in a sooting lifted turbulent ethylene/air non-premixed flame, Combust. Flame 179 (2017) 33 – 50.

[8] S.-Y. Lee, S. R. Turns, R. J. Santoro, Measurements of soot, OH, and PAH concentrations in turbulent ethylene/air jet flames, Combust. Flame 156 (12) (2009) 2264 – 2275.

[9] S. Mahmoud, G. Nathan, Z. Alwahabi, Z. Sun, P. Medwell, B. Dally, The effect of exit Reynolds number on soot volume fraction in turbulent non-premixed jet flames, Combust. Flame 187 (2018) 42 – 51.

[10] S. Mahmoud, G. Nathan, Z. Alwahabi, Z. Sun, P. Medwell, B. Dally, The effect of exit strain rate on soot volume fraction in turbulent non-premixed jet flames, Proc. Combust. Inst. 36 (1) (2017) 889 – 897.

[11] L.-Y. Wang, S. Chatterjee, Q. An, A. M. Steinberg, Ö. L. Gülder, Soot formation and flame structure in swirl-stabilized turbulent non-premixed methane combustion, Combust. Flame 209 (2019) 303 – 312.

[12] F. Bisetti, G. Blanquart, M. E. Mueller, H. Pitsch, On the formation and early evolution of soot in turbulent nonpremixed flames, Combust. Flame 159 (1) (2012) 317 – 335.

[13] A. Attili, F. Bisetti, M. E. Mueller, H. Pitsch, Damköhler number effects on soot formation and growth in turbulent nonpremixed flames, Proc. Combust. Inst. 35 (2) (2015) 1215 – 1223.

[14] O. Park, R. A. Burns, O. R. Buxton, N. T. Clemens, Mixture fraction, soot volume fraction, and velocity imaging in the soot-inception region of a turbulent non-premixed jet flame, Proc. Combust. Inst. 36 (1) (2017) 899 – 907.

[15] L. Cai, H. Pitsch, Optimized chemical mechanism for combustion of gasoline surrogate fuels, Combust. Flame 162 (5) (2015) 1623 – 1637.

[16] S. Kruse, A. Wick, P. Medwell, A. Attili, J. Beeckmann, H. Pitsch, Experimental and numerical study of soot formation in counterflow diffusion flames of gasoline surrogate components, Combust. Flame 210 (2019) 159 – 171.

[17] S. Kruse, J. Ye, Z. Sun, A. Attili, B. Dally, P. Medwell, H. Pitsch, Experimental investigation of soot evolution in a turbulent non-premixed prevaporized toluene flame, Proc. Combust. Inst. 37 (1) (2019) 849 – 857.

[18] M. J. Evans, P. R. Medwell, Z. Sun, A. Chinnici, J. Ye, Q. N. Chan, B. B. Dally, Downstream evolution of n-heptane/toluene flames in hot and vitiated coflows, Combust. Flame 202 (2019) 78 – 89.

[19] D. Gu, Z. Sun, G. J. Nathan, P. R. Medwell, Z. T. Alwahabi, B. B. Dally, Improvement of precision and accuracy of temperature imaging in sooting flames using two-line atomic fluorescence (TLAF), Combust. Flame 167 (2016) 481 – 493.

[20] Z. Sun, D. Gu, G. Nathan, Z. Alwahabi, B. Dally, Single-shot, Time-Resolved planar Laser-Induced Incandescence (TiRe-LII) for soot primary particle sizing in flames, Proc. Combust. Inst. 35 (3) (2015) 3673 – 3680.

[21] M. Mueller, G. Blanquart, H. Pitsch, Hybrid Method of Moments for modeling soot formation and growth, Combust. Flames 156 (6) (2009) 1143 – 1155.

[22] H. Pitsch, E. Riesmeier, N. Peters, Unsteady Flamelet Modeling of Soot Formation in Turbulent Diffusion Flames, Combus. Sci. Technol. 158 (1) (2000) 389–406.

[23] G. L. Hubbard, C. L. Tien, Infrared Mean Absorption Coefficients of Luminous Flames and Smoke, J. Heat Transfer 100 (2) (1978) 235–239.

[24] W. R. Hawthorne, D. S. Wedell, H. C. Hottelz, Mixing and Combustion in Turbulent Gas Jets, 3rd Symp. (Int.) Combust. (1949) 266–288.

[25] B. Franzelli, P. Scouflaire, S. Candel, Time-resolved spatial patterns and

interactions of soot, PAH and OH in a turbulent diffusion flame, Proc. Combust. Inst. 35 (2) (2015) 1921 – 1929.

[26] N. Qamar, Z. Alwahabi, Q. Chan, G. Nathan, D. Roekaerts, K. King, Soot volume fraction in a piloted turbulent jet non-premixed flame of natural gas, Combust. Flame 156 (7) (2009) 1339 – 1347.

[27] F. Liu, H. Guo, G. J. Smallwood, Ö. L. Gülder, Effects of gas and soot radiation on soot formation in a coflow laminar ethylene diffusion flame, J. Quant. Spectrosc. Radiat. Transfer 73 (2) (2002) 409 – 421.